SCIENCE CHINA
Earth Sciences

•ARTICLE•

January 2024 Vol.67 No.1: 105–116
https://doi.org/10.1007/s11430-023-1229-7

The importance of data assimilation components for initial conditions and subsequent error growth

Zhongrui WANG[1#], Haohao SUN[1#], Lili LEI[1,2*], Zhe-Min TAN[1] & Yi ZHANG[1]

[1] *Key Laboratory of Mesoscale Severe Weather, Ministry of Education, and School of Atmospheric Sciences, Nanjing University, Nanjing 210023, China;*
[2] *Frontiers Science Center for Critical Earth Material Cycling, Nanjing University, Nanjing 210023, China*

Received April 5, 2023; revised November 12, 2023; accepted November 21, 2023; published online December 15, 2023

Abstract Despite a specific data assimilation method, data assimilation (DA) in general can be decomposed into components of the prior information, observation forward operator that is given by the observation type, observation error covariances, and background error covariances. In a classic Lorenz model, the influences of the DA components on the initial conditions (ICs) and subsequent forecasts are systematically investigated, which could provide a theoretical basis for the design of DA for different scales of interests. The forecast errors undergo three typical stages: a slow growth stage from 0 h to 5 d, a fast growth stage from 5 d to around 15 d with significantly different error growth rates for ensemble and deterministic forecasts, and a saturation stage after 15 d. Assimilation strategies that provide more accurate ICs can improve the predictability. Cycling assimilation is superior to offline assimilation, and a flow-dependent background error covariance matrix ($\mathbf{P}^f$) provides better analyses than a static background error covariance matrix (**B**) for instantaneous observations and frequent time-averaged observations; but the opposite is true for infrequent time-averaged observations, since cycling simulation cannot construct informative priors when the model lacks predictive skills and the flow-dependent $\mathbf{P}^f$ cannot effectively extract information from low-informative observations as the static **B**. Instantaneous observations contain more information than time-averaged observations, thus the former is preferred, especially for infrequent observing systems. Moreover, ensemble forecasts have advantages over deterministic forecasts, and the advantages are enlarged with less informative observations and lower predictive-skill model priors.

Keywords Data assimilation, Atmospheric predictability, Background error covariances, Ensemble forecasts

Citation: Wang Z, Sun H, Lei L, Tan Z M, Zhang Y. 2024. The importance of data assimilation components for initial conditions and subsequent error growth. Science China Earth Sciences, 67(1): 105–116, https://doi.org/10.1007/s11430-023-1229-7

1. Introduction

Advanced data assimilation (DA) has been a major contributor to the improvements in numerical weather prediction (NWP; e.g., Courtier et al., 1994; Whitaker et al., 2008; Buehner et al., 2010; Bauer et al., 2015; Bannister, 2017) and climate prediction (e.g., Meehl et al., 2009; Karspeck et al., 2013, Massonnet et al.; 2013, Balsamo et al., 2012; Mochizuki et al., 2016). Based on the knowledge of uncertainties in the observation and prior information, DA seeks the best estimate of the dynamic system, which is often used as the initial condition (IC) for subsequent forecasts (e.g., Kalnay, 2002). Daily weather forecasts and Seasonal-Interannual (SI) climate predictions like the El Nino-Southern Oscillation (ENSO) forecasts can be seen as "initial value problems", but the importance of the initial value decays with forecast lead times (Meehl et al., 2009).

The Earth system is characterized by interactive and complex nonlinear dynamical and physical processes that span a wide range of spatial and temporal scales (e.g., Lucarini et al., 2014). To capture the features of the Earth

* Corresponding author (email: lililei@nju.edu.cn)
# The authors contributed equally to this work

system, seamless prediction that requires forecasts across the range of weather and climate time scales is required (Palmer et al., 2008; Shapiro et al., 2010; Ruti et al., 2020), and the ICs for predictions from days to decades are provided by DA for coupled Earth system models (Brunet et al., 2010). To predict the nonlinear dynamical and physical processes across time scales, coupled DA has been applied, especially for the significantly under-observed non-atmospheric components of the Earth system (e.g., Zhang, 2011; Yang et al., 2013; Jung et al., 2016; Laloyaux et al., 2016; Penny and Hamill, 2017). Tardif et al. (2014, 2015) showed that assimilating time-averaged atmospheric observations could improve the Atlantic meridional overturning circulation (AMOC), especially with insufficient oceanic observations. Lu et al. (2015a, 2015b) and Sun et al. (2020) proposed a leading averaged coupled covariance (LACC) method to effectively incorporate the observed fast atmospheric variables into the update of the oceanic variables. But research on how the observations from the components with slow time scales influence the atmosphere with fast time scales is limited.

Despite the challenge of seamless prediction from decadal to SI and then subseasonal-to-seasonal (S2S) predictions, NWP has the challenge to maintain the skill of weather forecasts and extend the skill to longer timescales. Lorenz (1969a, 1969b) demonstrated that the IC error in small scales induced error growth in large scales and the predictability depended on the equilibrium energy spectrum. The rapid upscale growth of IC errors through moist processes can limit the predictability of severe weather (Tan et al., 2004; Zhang, 2005), and the upscale error growth undergoes three stages with different characteristics from small scales to large scales (Zhang et al., 2007). There is evidence of predictability for some extreme weather events about 7–10 days in advance (Hamill et al., 2006), and also latitude-varying error growth characteristics that are consistent with the underlying dynamics of tropics, midlatitudes and polar regions (Judt, 2020). Zhang et al. (2019) showed that for the midlatitude weather, a skillful deterministic forecast lead time can be extended up to 15 d by reducing an order of the current IC error.

DA has been devoted to providing the most accurate IC for NWP. There have been dedicated efforts to assimilate various types of observations, including the satellite radiances (e.g., Geer et al., 2018; Li et al., 2021), GPS radio occultation (e.g., Cucurull et al., 2007; Poli et al., 2010), aircraft data (e.g., Cardinali et al., 2003; Tong et al., 2018), radar observations (e.g., Zhang et al., 2009; Zeng et al., 2021), etc. These advanced observations differ in local/non-local observed quantities, spatial coverages, and available frequencies. Meanwhile, the DA strategies have been vastly advanced, from the variational methods (e.g., Courtier et al., 1998; Rawlins et al., 2007) and ensemble Kalman filters (e.g., Whitaker et al., 2008; Houtekamer and Zhang, 2016) to the hybrid variants (e.g., Hamill and Snyder, 2000; Bannister, 2017). To capture the error statistics from small to large scales, multi-scale DA methods that often implement iterative assimilation or scale-dependent treatment for background error covariances have been developed (e.g., Xie et al., 2011; Li et al., 2015; Huang et al., 2021). However, there is a lack of knowledge for DA strategies that interact with observation types and influence subsequent error growths.

Different from most previous studies that mainly concentrate on the role of background error covariances for DA, this study decomposes the DA components into a broader view to investigate the influences of DA components on the IC error and subsequent error growth. No matter a variational method or an ensemble Kalman filter is used, there are mainly four DA components for obtaining the assimilated posterior, which are the prior information, observation forward operator that is given by the observation type, observation error covariances, and background error covariances. By designing different types of DA components, the influences of the DA components on the assimilated analysis and associated error growth are systematically analyzed within a coherent ensemble framework, based on the classic Lorenz (2005) model. The understanding of the importance of DA components on different scales could give a theoretical basis to design the appropriate DA strategy for the scales of interests.

2. Data assimilation components

Given the prior of state vector $\mathbf{x}^f$ and observation $\mathbf{y}$, the best estimate of state vector $\mathbf{x}^a$ has the equivalent form of $\mathbf{x}^a = \mathbf{x}^f + \mathbf{K}[\mathbf{y} - H(\mathbf{x}^f)]$, by applying either the three-dimensional variational method (3DVAR; Courtier et al., 1998) or ensemble Kalman filter (EnKF; Whitaker et al., 2008). H is the observation forward operator that transforms state variables to the observed quantities. The gain matrix $\mathbf{K}$ has the form of $\mathbf{K} = \mathbf{P}^f\mathbf{H}^{\mathrm{T}}\left(\mathbf{H}\mathbf{P}^f\mathbf{H}^{\mathrm{T}} + \mathbf{R}\right)^{-1}$, where $\mathbf{P}^f$ is the background error covariance matrix, $\mathbf{R}$ is the observation error covariance matrix, and $\mathbf{H}$ is the Jacobian matrix of observation forward operator that is the partial derivative of the forward operator with respect to the state variable.

Lei et al. (2021) showed that the ensemble Kalman filter (EnKF; Whitaker et al., 2008), three-dimensional variational method (3DVAR; Courtier et al., 1998), and hybrid ensemble-variational methods (Hamill and Snyder, 2000; Penny, 2014) can be implemented in an ensemble framework. This is done by separating the ensemble mean and perturbations and then sampling the static background error covariances through a large size of climatological ensemble perturbations. Let $\overline{\mathbf{x}}^f$ denotes the control prior information,

which can be a deterministic simulation or an ensemble mean from ensemble forecasts. A group of prior ensemble perturbations $\left[\mathbf{x}_1^{f'}, \mathbf{x}_2^{f'}, \ldots, \mathbf{x}_N^{f'}\right]$ where N is the ensemble size, can be generated by either sampling the climatological perturbations or performing short-term ensemble forecasts with subtraction of the ensemble mean. By adding the ensemble perturbations to the control prior, N prior ensemble members can be created, $\mathbf{x}_i^f = \overline{\mathbf{x}}^f + \mathbf{x}_i^{f'}$ (i=1,…, N). In the ensemble framework, an EnKF that incorporates observations $\mathbf{y}$ into the prior ensembles, gives the posterior ensemble mean and perturbations,

$$\begin{aligned}\overline{\mathbf{x}}^a &= \overline{\mathbf{x}}^f + \left\{\boldsymbol{X}(\mathbf{H}\boldsymbol{X})^{\mathrm{T}}\left[(\mathbf{H}\boldsymbol{X})(\mathbf{H}\boldsymbol{X})^{\mathrm{T}} + \mathbf{R}\right]^{-1}\right\}\left[\mathbf{y} - \overline{H(\mathbf{x}^f)}\right] \\ &= \overline{\mathbf{x}}^f + \left[\mathbf{P}^f\mathbf{H}^{\mathrm{T}}\left(\mathbf{H}\mathbf{P}^f\mathbf{H}^{\mathrm{T}} + \mathbf{R}\right)^{-1}\right]\left[\mathbf{y} - \overline{H(\mathbf{x}^f)}\right], \qquad (1)\end{aligned}$$

$$\begin{aligned}\mathbf{x}_i^{a'} &= \mathbf{x}_i^{f'} - \left\{\boldsymbol{X}(\mathbf{H}\boldsymbol{X})^{\mathrm{T}}\left[\left(\sqrt{(\mathbf{H}\boldsymbol{X})(\mathbf{H}\boldsymbol{X})^{\mathrm{T}} + \mathbf{R}}\right)^{-1}\right]^{\mathrm{T}}\right. \\ &\quad \left.\times\left[\sqrt{(\mathbf{H}\boldsymbol{X})(\mathbf{H}\boldsymbol{X})^{\mathrm{T}} + \mathbf{R}} + \sqrt{\mathbf{R}}\right]^{-1}\right\}\mathbf{H}\mathbf{x}_i^{f'} \\ &= \mathbf{x}_i^{f'} - \left\{\mathbf{P}^f\mathbf{H}^{\mathrm{T}}\left[\left(\sqrt{\mathbf{H}\mathbf{P}^f\mathbf{H}^{\mathrm{T}} + \mathbf{R}}\right)^{-1}\right]^{\mathrm{T}}\right. \\ &\quad \left.\times\left[\sqrt{\left(\mathbf{H}\mathbf{P}^f\mathbf{H}^{\mathrm{T}} + \mathbf{R}\right)} + \sqrt{\mathbf{R}}\right]^{-1}\right\}\mathbf{H}\mathbf{x}_i^{f'}. \qquad (2)\end{aligned}$$

The normalized prior ensemble perturbations $\boldsymbol{X} = \left[\mathbf{x}_1^{f'}, \mathbf{x}_2^{f'}, \ldots, \mathbf{x}_N^{f'}\right] / \sqrt{N-1}$ is the square root of the background error covariance matrix $\mathbf{P}^f$, since the multiplication of $\boldsymbol{X}$ and its transpose gives $\mathbf{P}^f = \boldsymbol{X}\boldsymbol{X}^{\mathrm{T}}$. Given the Jacobian matrix $\mathbf{H}$, $\mathbf{H}\boldsymbol{X}$ gives the normalized ensemble perturbations in the observation space.

Therefore, the DA given by eq.(1) and eq.(2) can be divided into four components: the prior information ($\mathbf{x}^f$), observation forward operator (H and $\mathbf{H}$), observation error covariances ($\mathbf{R}$), and background error covariances ($\mathbf{P}^f$). Different from previous studies that independently apply one DA method, the DA components can be mixed to provide the assimilation analyses, like building blocks. Thus the impact of each DA component on the analyses and subsequent forecasts can be independently and systematically examined.

NWP is an IC problem, since it relies on the accurately estimated current state to initialize the forecast (Kalnay, 2002). Thus the control prior $\overline{\mathbf{x}}^f$ is often generated from a cycling DA. That is, a short-term deterministic / ensemble forecast is performed from the posterior(s) obtained at the previous DA cycle. Thus the control prior contains information of all past observations, model dynamics, and physics (e.g., Kalnay, 2002; Bauer et al., 2015), which also indicates that the model has high predictive skills. But for climate simulations that have low predictive skills, especially for time scales longer than the temporal resolution of observations, the prior from the cycling DA might not be superior to those randomly drawn from climatological samples (e.g., Matsikaris et al., 2015; Sun et al., 2022). Thus the offline DA utilizes the prior that samples the climatological distribution of the state variable, which requires much less computational costs than the cycling DA since no model advances are needed after each assimilation. The prior choice of cycling (Cyc) and offline (Off) in Table 1 indicates a weather-/climate-type assimilation.

Similarly, the ensemble perturbations $\boldsymbol{X}$ can be generated from short-term ensemble forecasts that are launched from the ensemble posteriors, which provides the flow-dependent background error covariance matrix $\mathbf{P}^f$. The ensemble perturbations can also be created by sampling the climatological perturbations, and they approximate the static background error covariance matrix $\mathbf{B}$ that is often used by variational-based DA methods. Therefore, through the ensemble DA given by eq.(1) and eq.(2), a deterministic forecast $\overline{\mathbf{x}}^f$ and climatological ensemble perturbations $\boldsymbol{X}$ provide an equivalent solution to 3DVAR. If the control prior $\overline{\mathbf{x}}^f$ and ensemble perturbations $\boldsymbol{X}$ are obtained from the same ensemble forecasts, the solution of the traditional EnKF is obtained. A hybrid background error covariance matrix that is a combination of $\mathbf{B}$ and $\mathbf{P}^f$ is adopted by the hybrid DA methods. For simplicity, the choice of background error covariance matrix shown in Table 1 is either the static $\mathbf{B}$ (B) or flow-dependent $\mathbf{P}^f$ (Pb). As shown by eq.(1) and eq.(2), the assimilation increment is influenced by the relative weight of the background error covariance matrix compared to the observation error covariance matrix, and thus with an emphasis on the background error covariance matrix, the sensitivity of the observation error covariance matrix on DA and forecasts is not discussed here.

No matter whether the control prior is from a cycling or an offline DA, the control prior can be either a deterministic one or an ensemble mean from ensemble members. Meanwhile, when the state update is accomplished, forecasts can be launched from the posteriors produced by DA. If a deterministic control prior is applied, a deterministic forecast can be launched from the posterior; otherwise, ensemble forecasts can be launched from the ensemble analyses. Two forecast kinds, deterministic (Det) and ensemble (Ens), are shown in Table 1. Ensemble forecasts of the assimilation experiments with cross components (e.g., ensemble cycling assimilation with static $\mathbf{B}$ and ensemble offline assimilation with flow-dependent $\mathbf{P}^f$) are not conducted, since it is unlikely to use full static $\mathbf{B}$ if an ensemble forecast is available and also it is impractical to launch an ensemble forecast from an offline assimilation.

To examine the observations with different scales, two sets of observation types are designed. One set is in-

Table 1 Configurations of the data assimilation experiments [a)]

Exp. Name	DA cycle	Background error covariance matrix	Observation type	Forecast kind
Cyc_Pb_Ens_Inst_*x*	Cycling	Flow-dependent $\mathbf{P}^f$	Instantaneous	Ensemble
Cyc_Pb_Det_Inst_*x*	Cycling	Flow-dependent $\mathbf{P}^f$	Instantaneous	Deterministic
Cyc_B_Det_Inst_*x*	Cycling	Static **B**	Instantaneous	Deterministic
Off_Pb_Det_Inst_*x*	Offline	Flow-dependent $\mathbf{P}^f$	Instantaneous	Deterministic
Off_B_Ens_Inst_*x*	Offline	Static **B**	Instantaneous	Ensemble
Off_B_Det_Inst_*x*	Offline	Static **B**	Instantaneous	Deterministic
Cyc_Pb_Ens_Tavg_*x*	Cycling	Flow-dependent $\mathbf{P}^f$	Time-averaged	Ensemble
Cyc_Pb_Det_Tavg_*x*	Cycling	Flow-dependent $\mathbf{P}^f$	Time-averaged	Deterministic
Cyc_B_Det_Tavg_*x*	Cycling	Static **B**	Time-averaged	Deterministic
Off_Pb_Det_Tavg_*x*	Offline	Flow-dependent $\mathbf{P}^f$	Time-averaged	Deterministic
Off_B_Ens_Tavg_*x*	Offline	Static **B**	Time-averaged	Ensemble
Off_B_Det_Tavg_*x*	Offline	Static **B**	Time-averaged	Deterministic

a) The *x* in the experiment name indicates the observing frequency, including 6 h, 1 d, 5 d, and 10 d

stantaneous observations that observe the gridded values at a given time, which are analogous to conventional weather observations. The other set is time-averaged observations that observe the temporally averaged grid values over a certain time window, which simulate the observations with longer time scales than the instantaneous ones, like the sea surface temperature. The observation forward operator and its Jacobian for the instantaneous ones are a spatial interpolation, and for the time-averaged ones are a spatio-temporal interpolation. The observation types of instantaneous (Inst) and time-averaged (Tavg) in Table 1 indicate atmospheric-/oceanic-type observations. The time-averaged observations approach to the instantaneous ones as the observation frequency increases.

3. Experimental design

The one-scale model II of Lorenz (2005) model is adopted to examine the impacts of DA components on the analyses and forecasts. It simulates the behavior of a scalar atmospheric quantity at one level and one latitude with well represented atmospheric wavelengths and error-growth rates, and has been widely used for DA developments (e.g., Brajard et al., 2020; Lei et al., 2021). The one-scale model II of Lorenz (2005) with 960 grid points is governed by

$$\frac{\mathrm{d}X_n}{\mathrm{d}t} = [X,X]_{K,n} - X_n + F, \tag{3}$$

where the subscript n indexes the grid point, K and F are constant parameters that are set to 32 and 16, respectively. The advection term $[X,X]_{K,n}$ is formulated by

$$[X,X]_{K,n} = -W_{n-2K}W_{n-K} + \sum_{j=-J}^{J}{}' W_{n-K+j}X_{n+K+j}/K, \tag{4}$$

where $W_n = \sum_{i=-J}^{J}{}' X_{n-i}/K$ with $J=K/2$ when K is even and $W_n = \sum_{i=-J}^{J} X_{n-i}/K$ with $J=(K-1)/2$ when K is odd. The special sum $\sum'$ is the same as the ordinary sum except that the first and last terms are divided by 2.

The observing simulation system experiments with a perfect-model assumption are conducted, in which the same model configurations are used for the nature run and simulations. ICs of the nature run, deterministic and ensemble simulations are randomly drawn from a large set of independent states. Synthetic observations are created by adding random perturbations drawn from a normal distribution $N(0, R)$ to the true values from the nature run. Two sets of observations are generated, and both have the observing network of every 8 grid points and observation error variance R of 2.0. The instantaneous observation observes the gridded value at the middle of an assimilation window, and the time-averaged observation observes the temporally averaged value over an assimilation window. The observation density and error variance are chosen as an intermediate range for the observing networks of weather and climate. The observing frequencies vary from 6 h, 1 d, 5 d, to 10 d, respectively. Note that for the dimensionless time unit of the Lorenz (2005) model, 0.05 is approximately 6 h. The assimilation window is set to the same as the observing frequency, so that more observations are assimilated when the observing frequency increases, which would directly reduce the analysis error.

The ensemble size of ensemble-based DA and ensemble forecasts is 40. To combat sampling errors resulting from a limited ensemble size, covariance inflation and covariance localization are applied for assimilation experiments with flow-dependent background error covariance matrix $\mathbf{P}^f$. The constant multiplicative inflation (Anderson and Anderson, 1999) is applied to enlarge the ensemble spread and prevent filter divergence. The Gaspari and Cohn (GC; Gaspari and Cohn, 1999) function is used to localize the impact of observations and mitigate the spurious error correlations between observations and state variables. The inflation and localization parameters are tuned to be optimal for each assimilation experiment. But no covariance inflation and localization are applied for the assimilation experiments with static background error covariance matrix **B**, since sufficiently large sizes of climatological perturbations are used to estimate the static **B**. The sample sizes of climatological perturbations for instantaneous observations with varying frequencies and time-averaged observations with 6-hour and 1-day frequencies, are on the order of 10^4. For time-averaged observations with 5-day and 10-day frequencies, the sample sizes are on the order of 10^3 due to the time averaging.

DA experiments are conducted for 500 d, and the first 50-d assimilations are discarded to avoid transients. The deterministic posterior or ensemble mean of the ensemble posteriors from DA experiments of the remaining 450 d is first verified relative to the natural run. To examine the impact of DA components on forecasts, free forecasts are launched from the assimilation analyses. To have the same forecast samples for different DA windows, the free forecast is launched every 10 d from the middle of a DA window for the remaining 450 d, and thus a single forecast period is half a DA window plus 20 d. The schematic of DA experiments is shown by Figure 1. The deterministic forecast or ensemble mean of the ensemble forecasts is verified against the nature run every 6 h. Spatially and temporally averaged root-mean-square (RMS) error is computed for verification. To examine the significance among the error differences, a paired sample *t*-test is performed based on the 45 samples (every 10 d from the 450-d verification period), and the error difference is statistically significant given by the 99% confidence level. Different DA experiments have forecast errors growing differently, due to the different ICs provided by the DA components. To fairly compare the error growth given different DA components, the starting point of each forecast error curve is adjusted to the time at which the initial error is closest to the error of the reference experiment. The groups of DA experiments and the associated reference experiment are introduced in the main text. The error growth is divided into three stages: the first one is from 0 h to 5 d, the second one is from 5 d to around 15 d, and the last one is the saturation stage that is approximately longer than 15 d. The end date of the second error growth stage is objectively given by the smallest error of the linear regression.

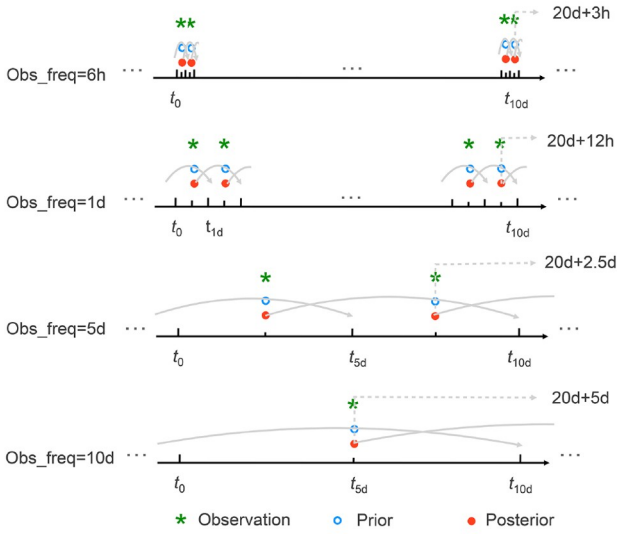

Figure 1 Schematic of DA experiments with observing frequencies of 6 h, 1 d, 5 d and 10 d, respectively. Solid gray lines denote the cycling assimilation and forecast, and the dashed lines show the free forecast launched every 10 d with a forecast lead time of 20 d plus half the DA window.

4. Impacts of DA components on posteriors

Through deterministic or ensemble cycling assimilation of the instantaneous observations with flow-dependent background error covariance matrix $\mathbf{P}^f$ (Cyc_Pb_Det_Inst and Cyc_Pb_Ens_Inst), the posterior RMS errors increase with decreased observing frequency, since less observation information is available when the observation becomes more infrequent (Figure 2a and Table 2). The posterior errors of deterministic cycling assimilation with static **B** (Cyc_B_Det_Inst) increase with decreased observing frequency. The posterior errors of deterministic cycling assimilation with static **B** are generally significantly increased compared to those of deterministic cycling assimilation with flow-dependent $\mathbf{P}^f$, especially for frequent observations. For either the cycling assimilations with flow-dependent $\mathbf{P}^f$ or offline assimilations with static **B**, the posterior errors with ensemble simulations are significantly smaller than those of deterministic ones. Given each observing frequency, the posterior errors of deterministic/ensemble offline assimilation with static **B** (Off_B_Det_Inst/Off_B_Ens_Inst) are in general slightly increased compared to those of deterministic cycling assimilation with static **B**, while the differences are statistically significant with frequent observations (6 h and 1 d). The posterior errors of deterministic offline assimilation with flow-dependent $\mathbf{P}^f$ (Off_Pb_Det_Inst) are significantly larger than the others, especially for frequent observations. This is because the prior error is about the climatological error due to the offline sampling, but the flow-

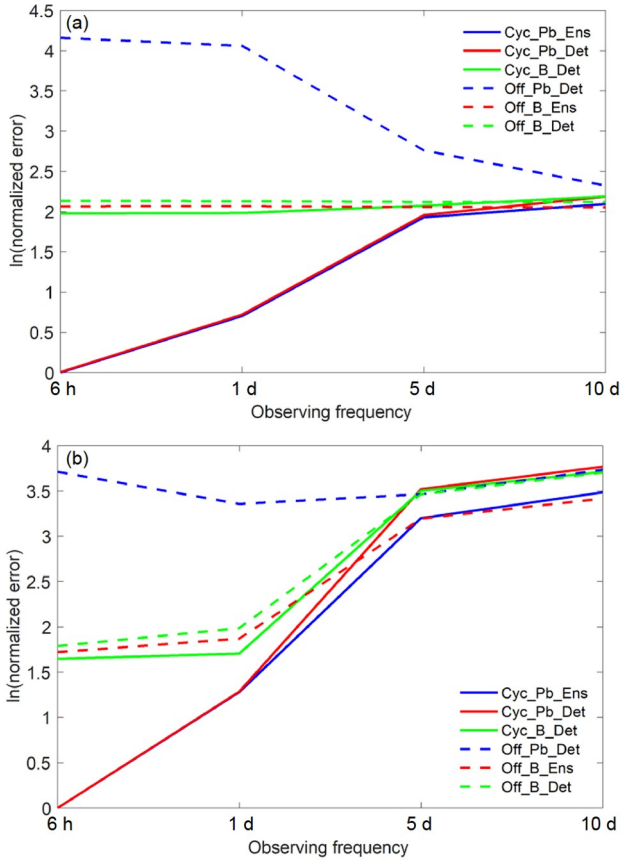

Figure 2 The natural logarithm of the posterior errors from DA experiments with different observing frequencies normalized by that of the reference experiment Cyc_Pb_Ens_6h, for (a) instantaneous observations and (b) time-averaged observations. Specific values of the posterior errors are shown in Table 2.

dependent $\mathbf{P}^f$ obtained from the cycling ensemble has a much smaller spread than the climatological one, so that the insufficient ensemble spread cannot accurately represent the prior uncertainty and results in too small increments. Thus for instantaneous observations with different observing frequencies, ensemble simulations are beneficial compared to deterministic simulations, and the cycling assimilation has advantages over offline assimilation. And most importantly, flow-dependent $\mathbf{P}^f$ has significant impacts on the analyses compared to static **B**, especially for frequent observations.

Similar results to the assimilation of instantaneous observations are generally obtained for the assimilation of time-averaged observations (Figure 2b and Table 2). For each assimilation configuration, assimilating the time-averaged observations generally has significantly larger posterior errors than assimilating the instantaneous ones, especially with infrequent observations. This indicates that time-averaged observations contain less information than the instantaneous ones, and the observation information is further reduced with increased averaging length. The advantages of ensemble simulations over deterministic simulations are much enlarged by assimilating the time-averaged observations compared to the instantaneous ones with infrequent observations (5 d and 10 d). This is consistent with Sun et al. (2022), since the model has low predictive skills when the forecast lead time is large and observations are infrequent, and then ensemble averaging becomes essential for constructing an informed prior. When assimilating infrequent time-averaged observations, using a static **B** instead of flow-dependent $\mathbf{P}^f$, and using offline assimilation instead of cycling assimilation, result in significantly smaller posterior errors, which is different from the previous assimilation of frequent instantaneous observations. This is because when the model lacks predictive skills and observations contain information averaged over a relatively long time period, cycling simulations cannot construct more informed priors compared to random samples from the climatological dis-

Table 2 Posterior errors of each data assimilation configuration with different observing frequencies

Observing frequency	6 h	1 d	5 d	10 d
Cyc_Pb_Ens_Inst	0.1347	0.2717	0.9271	1.0942
Cyc_Pb_Det_Inst	0.1356	0.2768	0.9539	1.1995
Cyc_B_Det_Inst	0.9722	0.9782	1.0699	1.2029
Off_Pb_Det_Inst	8.6262	7.8057	2.1304	1.3742
Off_B_Ens_Inst	1.0615	1.0639	1.0519	1.0494
Off_B_Det_Inst	1.1371	1.1342	1.1219	1.1205
Cyc_Pb_Ens_Tavg	0.1910	0.6863	4.6809	6.2307
Cyc_Pb_Det_Tavg	0.1912	0.6904	6.4494	8.2697
Cyc_B_Det_Tavg	0.9923	1.0501	6.3407	7.8168
Off_Pb_Det_Tavg	7.8179	5.4851	6.0992	7.9959
Off_B_Ens_Tavg	1.0672	1.2390	4.6599	5.8193
Off_B_Det_Tavg	1.1420	1.3916	6.0949	7.7589

tribution, and also the sample-estimated flow-dependent $\mathbf{P}^f$ cannot extract observation information as well as the static **B**. Thus given an infrequent observing system, instantaneous observations are preferred compared to time-averaged observations. To better extract information from the infrequent time-averaged observations, ensemble priors are necessary, and offline assimilation and static **B** have advantages over cycling assimilation and flow-dependent $\mathbf{P}^f$.

5. Impacts of DA components on error growth

5.1 Cycling assimilation with flow-dependent $\mathbf{P}^f$

The spatially averaged forecast errors of DA experiments with cycling assimilation of instantaneous observations using the flow-dependent background error covariance matrix $\mathbf{P}^f$ (Cyc_Pb_Ens_Inst and Cyc_Pb_Det_Inst) are shifted to the time at which the posterior errors are closest to the error of the reference experiment Cyc_Pb_Ens_Inst_6h, since the posterior errors differ with various observing frequencies. The spatially averaged forecast errors undergo three typical stages (Figure 3a). Forecast errors for each model grid point have similar patterns to the spatially averaged ones, and consistent results are obtained with ensemble mean errors and ensemble spread for the experiments with ensemble forecasts (Figures are not shown). Given the 6-h and 1-d observing frequencies, the ICs, *i.e.*, posteriors, have errors of $O(10^{-1})$, and errors slowly grow at a rate of 0.0069 h^{-1} till 5 d. At 5 d, forecast errors of DA experiments with 6-h and 1-d observing frequencies and IC errors of DA experiments with 5-d and 10-d observing frequencies have magnitudes of $O(10^0)$; from 5 d to about 15 d, forecast errors grow differently for deterministic and ensemble forecasts. Ensemble forecasts have an error growth rate of 0.0238 h^{-1}, while deterministic forecasts have an error growth rate of 0.0318 h^{-1}, which is 33.6% faster than that of ensemble forecasts. The advantages of ensemble simulations over deterministic simulations are much more prominent for the forecasts than the analyses. After about 15 d, forecast errors of deterministic and ensemble forecasts gradually saturate, approaching the climatological errors that are 8.55 and 6.16 for deterministic and ensemble forecasts, respectively. This is as expected, since the variance of the ensemble mean is N times smaller than that of one deterministic forecast, when the error approaches saturation. Ensemble (deterministic) forecasts have errors growing to 95% of the climatological error at 384 h (432 h).

A similar three-stage error growth is shown by cycling assimilation of time-averaged observations with flow-dependent $\mathbf{P}^f$ (Cyc_Pb_Ens_Tavg and Cyc_Pb_Det_Tavg), as shown by Figure 3b. The IC given a 6-h observing frequency has an error of $O(10^{-1})$, from which the forecast error slowly grows at a rate of 0.0101 h^{-1} till 5 d. This error growth rate is

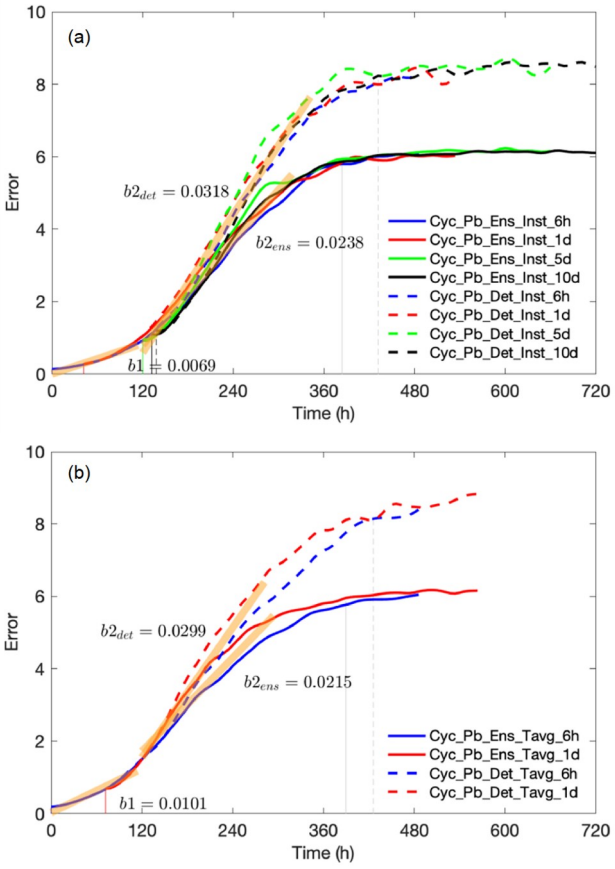

Figure 3 Forecast errors of cycling DA experiments with flow-dependent $\mathbf{P}^f$, using (a) instantaneous and (b) time-averaged observations. Solid and dashed lines denote the ensemble and deterministic forecasts, respectively. Blue, red, green, and black indicate the observing frequency of 6 h, 1 d, 5 d, and 10 d, respectively. Thick orange lines are the linear regression with slopes noted aside. Straight gray solid and dashed lines indicate the time at which the mean error of DA experiments approaches 95% of the climatological error of ensemble and deterministic forecasts, respectively. The other straight lines label the time when the posterior RMS error of according experiment is approximately the same as the error of the reference experiments Cyc_Pb_Ens_Inst_6h in (a) and Cyc_Pb_Ens_Tavg_6h in (b).

larger than that of assimilating instantaneous observations, because the IC error with 6-h time-averaged observations is slightly but significantly larger than that with 6-h instantaneous observations. At 5 d, forecast errors of DA experiments with 6-h and 1-d observing frequencies have magnitudes of $O(10^0)$; and from 5 d to about 15 d, forecast errors of ensemble and deterministic forecasts grow at rates of 0.0215 h^{-1} and 0.0299 h^{-1}, respectively. The error growth rates of the second stage from assimilating time-averaged observations are smaller than those from assimilating instantaneous observations, because the errors at 5 d from assimilating time-averaged observations are larger than those from assimilating instantaneous observations. The error growth rate of deterministic forecast is 39.1% faster than that of ensemble forecast. The advantages of ensemble simulations over deterministic simulations are kept with assimilation of time-averaged observations. After 15 d, the forecast

errors of deterministic and ensemble forecasts gradually approach the climatological errors. At 390 h (426 h), forecast errors of ensemble (deterministic) forecasts reach 95% of the climatological error. Forecast errors saturate at similar lead times for both instantaneous and time-averaged observations with different observing frequencies.

Different from the instantaneous observations, cycling assimilations of infrequent time-averaged observations (*i.e.*, 5-d and 10-d observing frequencies) with flow-dependent $\mathbf{P}^f$ (Cyc_Pb_Ens_Tavg and Cyc_Pb_Det_Tavg) provide ICs with errors much larger than those assimilating instantaneous observations (Figure 4). Similar results are obtained for different assimilation configurations with time-averaged observations, including cycling assimilation with static **B** and offline assimilation with either flow-dependent $\mathbf{P}^f$ or static **B** (Figure 4). Due to the large IC errors by assimilating the 5-d and 10-d time-averaged observations, forecast errors quickly saturate to the climatological errors. Thus no matter the assimilation strategy, forecast errors of assimilating time-averaged observations with 5-d and 10-d observing frequencies do not experience the first two error growth stages.

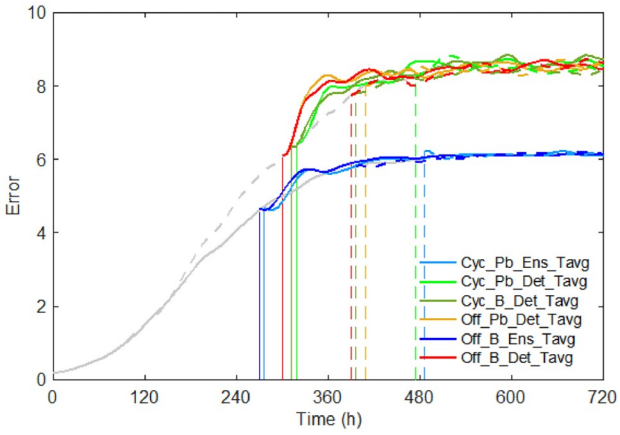

Figure 4 Forecast RMS errors of experiments assimilating time-averaged observations for observing frequency of 5 d (solid) and 10 d (dashed), respectively. The gray solid and dashed lines denote the reference experiments of 6-h cycling experiments with flow-dependent $\mathbf{P}^f$, using ensemble and deterministic forecasts, respectively. The straight lines label the time at which the posterior RMS error of according experiment is approximately the same as the RMS error of the reference experiment.

5.2 Offline assimilation with static B

Instead of having increased posterior RMS errors with lower observing frequencies as in the cycling assimilation with flow-dependent background error covariance matrix $\mathbf{P}^f$ (Figure 3), offline assimilation experiments with static **B** have similar posterior RMS errors for instantaneous observations with observing frequencies from 6 h to 10 d and time-averaged observations with observing frequencies of 6 h and 1 d (Off_B_Ens_Inst and Off_B_Det_Inst), as shown by Figure 5. By shifting the forecast errors of offline assimilation experiments with static **B** to the time at which the posterior error is closest to the RMS error of the reference experiment Cyc_Pb_Ens_Inst_6h (Figure 5a) and Cyc_Pb_Ens_Tavg_6h (Figure 5b) respectively, the forecast errors undergo the second and third stages, without the first stage of the reference experiments (Figure 3). The ICs of offline assimilation with static **B** for both instantaneous and time-averaged observations have errors of $O(10^0)$, which is an order larger than the IC errors of cycling assimilation with flow-dependent $\mathbf{P}^f$. Thus forecast errors of offline assimilation experiments with static **B** do not experience the first error growth stage as shown in Figure 3. From 5 d to about 15 d, forecast errors grow differently for deterministic and ensemble forecasts. By assimilating instantaneous observations, forecast error growth rates are 0.0268 h^{-1} and 0.0346 h^{-1} for ensemble and deterministic forecasts. By assimilating time-averaged observations, forecast errors grow at rates of 0.0296 h^{-1} and 0.0386 h^{-1} for ensemble and deterministic forecasts. The error growth rates of deterministic forecasts are 29.1% and 30.4% faster than that of ensemble forecasts for instantaneous and time-averaged observations, respectively. Ensemble simulations are also beneficial compared to deterministic simulations using offline assimilation with static **B**. The error growth rates of the second stage from offline assimilation with static **B** are larger than those from cycling assimilation with flow-dependent $\mathbf{P}^f$. Thus cycling assimilation with flow-dependent $\mathbf{P}^f$ can better constrain the error growth than offline assimilation with static **B**. Similar to cycling assimilation with flow-dependent $\mathbf{P}^f$, forecast errors of offline assimilation with static **B** gradually saturate after 15 d, approaching the climatological errors for deterministic and ensemble forecasts, respectively.

5.3 Assimilation with cross components

Compared to cycling assimilation with flow-dependent background error covariance matrix $\mathbf{P}^f$ and offline assimilation with static **B**, cycling assimilation can incorporate static **B**, while offline assimilation can utilize flow-dependent $\mathbf{P}^f$. Forecast errors of deterministic cycling assimilation with static **B** (Cyc_B_Det_Inst/Tavg) and deterministic offline assimilation with flow-dependent $\mathbf{P}^f$ (Off_Pb_Det_Inst/Tavg) are shifted to the time at which the posterior error is closest to the RMS error of the reference experiment Cyc_Pb_Det_Inst_6h (Figure 6a) and Cyc_Pb_Det_Tavg_6h (Figure 6b) respectively. Forecast errors with cross assimilation components are similar to those of deterministic forecasts from offline assimilation using static **B**, except for frequent instantaneous / time-averaged observations using offline assimilation with flow-dependent $\mathbf{P}^f$ due to large IC errors as previously discussed. Forecast errors undergo the second and third growth stages. The ICs of DA experiments with cross assimilation components have errors of $O(10^0)$,

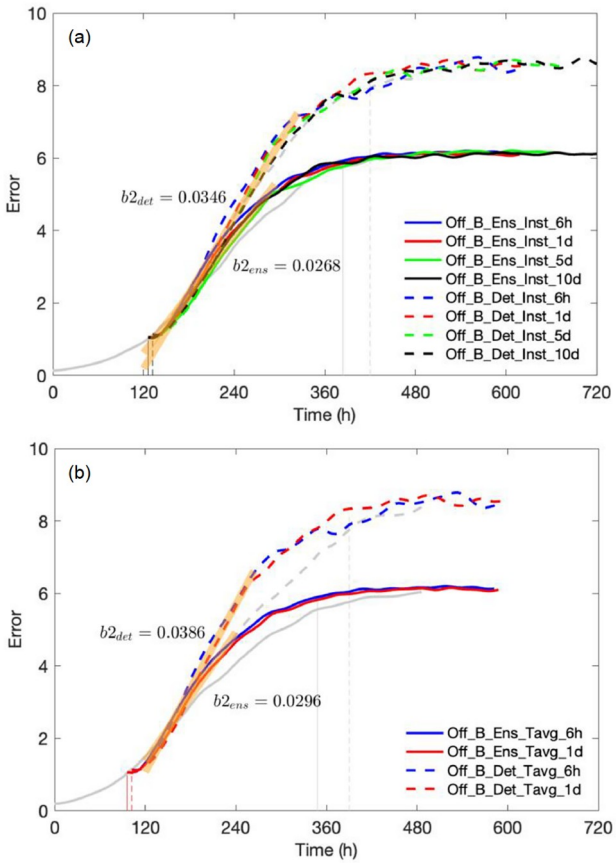

Figure 5 Same as Figure 3, except for offline ensemble DA with static **B** using (a) instantaneous and (b) time-averaged observations. The gray solid and dashed lines denote the reference experiments of 6-h cycling experiments with flow-dependent $\mathbf{P}^f$, using ensemble and deterministic forecasts, respectively.

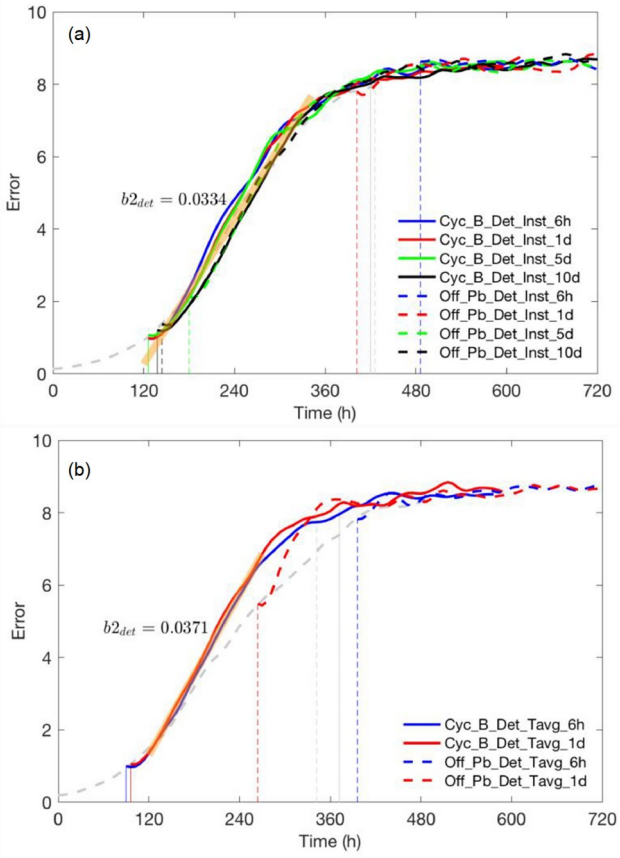

Figure 6 Forecast RMS errors of deterministic cycling assimilation with cross data assimilation components using (a) instantaneous and (b) time-averaged observations. Thick orange lines are the linear regression with slopes noted aside. Straight gray lines indicate the time at which the RMS error of deterministic cycling assimilation with static **B** (solid) and deterministic offline assimilation with flow-dependent $\mathbf{P}^f$ (dashed) approaches 95% of the climatological error. The other straight lines label the time when the posterior RMS error of according experiment is approximately the same as the RMS error of the reference experiment of 6-h cycling experiments with flow-dependent $\mathbf{P}^f$ using deterministic forecast.

thus the first error growth stage of cycling assimilation with flow-dependent $\mathbf{P}^f$ is not experienced. From 5 d to about 15 d, deterministic forecast errors grow at rates of 0.0334 h^{-1} and 0.0371 h^{-1} for instantaneous and time-averaged observations, respectively. The error growth rates are similar to those of offline assimilation with static **B**. After 15 d, deterministic forecast errors of DA experiments with cross assimilation components gradually saturate, approaching the climatological error of deterministic forecasts.

DA experiments with offline assimilation using static **B** and with cross assimilation components have IC whose errors are at least an order larger than those with cycling assimilation using flow-dependent $\mathbf{P}^f$. Thus the first stage of slow error growth from cycling assimilation using flow-dependent $\mathbf{P}^f$ is not experienced by the other assimilation configurations. DA experiments with offline assimilation using static **B** and with cross assimilation components undergo the second and third error growth stages similar to those of cycling assimilation using flow-dependent $\mathbf{P}^f$, and the former has a larger error growth rate of the second stage than the latter. Thus during the second stage, error growth can be better constrained by using cycling assimilation with flow-dependent $\mathbf{P}^f$ than the other assimilation configurations.

6. Discussions and conclusions

To understand the influences of data assimilation (DA) on the analysis and subsequent error growth without the limit of a specific DA method, the DA components are decomposed in a broader review, including the prior information, observation forward operator, observation error covariances, and background error covariances. The relative weight of the background error covariances to the observation error covariances gives the magnitude of the assimilation increment, and thus the background error covariances, along with the prior information and observation forward operator, are systematically investigated using the model II of Lorenz (2005).

In the model II of Lorenz (2005), the forecast errors un-

dergo three typical stages with IC errors of O(10^{-1}): from 0 h to 5 d, forecast errors slowly grow at a rate less than 0.01 h^{-1}; from 5 d to about 15 d, forecast errors fast grow at a rate of approximately 0.02 h^{-1} for ensemble forecasts and 0.03 h^{-1} for deterministic forecasts; after 15 d, forecast errors are approaching saturate to the climatological errors. The predictability can be gained by the assimilation strategies that provide more accurate ICs. With frequent observations, the IC errors of cycling assimilation with flow-dependent $\mathbf{P}^f$ are an order smaller than those of offline assimilation with static **B** and cross assimilation components (cycling assimilation with static **B** and offline assimilation with flow-dependent $\mathbf{P}^f$), thus the predictability of cycling assimilation with flow-dependent $\mathbf{P}^f$ extends 5 d compared to the other assimilation configurations. But with very low-informative observations (e.g., 5-d or10-d time-averaged observations), there is nearly no room for extending the predictability, since the ICs cannot be well constrained by any assimilation configurations here. Moreover, since the errors slowly grow during the first stage, substantial achievement of predictability for short-term forecasts can be expected by pushing the limit to improve the IC accuracy.

The prior information can be constructed from a deterministic simulation or ensemble ones, with a cycling or offline configuration. No matter the other assimilation configurations, ensemble simulations have advantages over deterministic simulations for the analysis, and the advantages are enlarged with less informative observations and lower predictive-skill priors. Ensemble forecasts also have advantages over deterministic forecasts, while the advantages of forecasts are more prominent than those of analyses with the maximum advantage approaches when the forecast error saturates. Meanwhile, cycling assimilation is superior to offline assimilation for frequent observations, but the opposite is generally true for infrequent observations. This is because when the model lacks predictive skills with barely informative observations, cycling simulation cannot construct more informed priors compared to random samples drawn from the climatological distribution. Thus the importance of cycling assimilation decreases with increased time scales of the dynamical system.

The background error covariances can be either the flow-dependent $\mathbf{P}^f$ or static **B**. With cycling assimilation, *i.e.*, more informative priors, the flow-dependent $\mathbf{P}^f$ generally provides better analyses than the static **B**, which indicates the sample estimated flow-dependent $\mathbf{P}^f$ better extracting observation information than the static **B**. But with offline assimilations, *i.e.*, less informative priors, the static **B** generally produces better analyses than the flow-dependent $\mathbf{P}^f$, which indicates the static **B** better extracting observation information than the sample estimated flow-dependent $\mathbf{P}^f$. The forecast error growth rates of the second stage are similar between offline assimilation with static **B** and cross assimilation components, while they are larger than those from cycling assimilation with flow-dependent $\mathbf{P}^f$. Thus cycling assimilation with flow-dependent $\mathbf{P}^f$ can better constrain the error growth than offline assimilation with static **B** and cross assimilation components.

Regarding to the observation forward operator (*i.e.*, the observation type), time-averaged observations with temporal averaging from 6 h to 10 d contain less information than instantaneous observations. With an increased averaging window, *i.e.*, less observing frequency, the information loss increases, as well as the loss of model predictability. The forecast error growth rate for the second stage is decided by the IC error at the beginning of the stage and the time duration of the stage. Given different configurations of the other assimilation components, time-averaged observations either have larger IC errors at the beginning of the stage (Figure 3) or have a shorter time duration of the stage (Figures 5 and 6) than instantaneous observations. Thus instantaneous observations are preferred compared to time-averaged observations, especially for infrequent observing systems. These results might not be suitable for situations with much more frequent observations, e.g., from minutes to seconds, in which high-frequent fluctuations could result in large observation noises and contaminate the additional observation information gained by more frequent observing.

Besides the four DA components discussed here, model error is also an important component for DA, whose impacts on DA and subsequent forecasts need further investigation. The influences of DA components on the analyses and forecasts are associated with the model predictive skills, and thus the importance of DA components on a coupled model is worthwhile to explore. Moreover, a classic but simple Lorenz model is used here, the importance of DA components needs be examined for realistic models.

Acknowledgements *The code that is used to generate the nature run, synthetic observations, and assimilation experiments, and the output of assimilation experiments with different assimilation configurations are available at https://meso.nju.edu.cn/xwdt/20220718/i226029.html. This work was supported by the National Natural Science Foundation of China (Grant Nos. 42192553, 41922036 & 41775057), the Frontiers Science Center for Critical Earth Material Cycling Fund (Grant No. JBGS2102), and the Fundamental Research Funds for the Central Universities (Grant No. 0209-14380097).*

Conflict of interest The authors declare that there are no conflicts of interest.

References

Anderson J L, Anderson S L. 1999. A Monte Carlo implementation of the nonlinear filtering problem to produce ensemble assimilations and forecasts. Mon Wea Rev, 127: 2741–2758

Balsamo G, Albergel A, Beljaars A, Boussetta S, Brun E, Cloke H L, Dee D. 2012. ERA-Interim/Land: A global land-surface reanalysis based on ERA-Interim meteorological forcing. ERA-Report series: 13

Bannister R N. 2017. A review of operational methods of variational and ensemble-variational data assimilation. Quart J R Meteoro Soc, 143: 607–633
Bauer P, Thorpe A, Brunet G. 2015. The quiet revolution of numerical weather prediction. Nature, 525: 47–55
Brajard J, Carrassi A, Bocquet M, Bertino L. 2020. Combining data assimilation and machine learning to emulate a dynamical model from sparse and noisy observations: A case study with the Lorenz 96 model. J Comput Sci, 44: 101171
Brunet G, Shapiro M, Hoskins B, Moncrieff M, Dole R, Kiladis G N, Kirtman B, Lorenc A, Mills B, Morss R, Polavarapu S, Rogers D, Schaake J, Shukla J. 2010. Collaboration of the weather and climate communities to advance subseasonal-to-seasonal prediction. Bull Amer Meteor Soc, 91: 1397–1406
Buehner M, Houtekamer P L, Charette C, Mitchell H L, He B. 2010. Intercomparison of variational data assimilation and the ensemble Kalman filter for global deterministic NWP. Part I: Description and single-observation experiments. Mon Weather Rev, 138: 1550–1566
Cardinali C, Isaksen L, Andersson E. 2003. Use and impact of automated aircraft data in a global 4DVAR data assimilation system. Mon Weather Rev, 131: 1865–1877
Courtier P, Thepaut J N, Hollingsworth A. 1994. A strategy for operational implementation of 4D-Var, using an incremental approach. Quart J R Meteorol Soc, 120: 1367–1387
Courtier P, Andersson E, Heckley W, Vasiljevic D, Hamrud M, Hollingsworth A, Rabier F, Fisher M, Pailleux J. 1998. The ECMWF implementation of three-dimensional variational assimilation (3D-Var). I: Formulation. Quart J R Meteoro Soc, 124: 1783–1807
Cucurull L, Derber J C, Treadon R, Purser R J. 2007. Assimilation of Global Positioning System radio occultation observations into NCEP's global data assimilation system. Mon Weather Rev, 135: 3174–3193
Gaspari G, Cohn S E. 1999. Construction of correlation functions in two and three dimensions. Quart J R Meteoro Soc, 125: 723–757
Geer A J, Lonitz K, Weston P, Kazumori M, Okamoto K, Zhu Y, Liu E H, Collard A, Bell W, Migliorini S, Chambon P, Fourrié N, Kim M, Köpken-Watts C, Schraff C. 2018. All-sky satellite data assimilation at operational weather forecasting centres. Quart J R Meteoro Soc, 144: 1191–1217
Hamill T M, Snyder C. 2000. A hybrid ensemble Kalman filter–3D variational analysis scheme. Mon Wea Rev, 128: 2905–2919
Hamill T M, Whitaker J S, Mullen S L. 2006. Reforecasts: An important dataset for improving weather predictions. Bull Amer Meteor Soc, 87: 33–46
Houtekamer P L, Zhang F. 2016. Review of the ensemble kalman filter for atmospheric data assimilation. Mon Weather Rev, 144: 4489–4532
Huang B, Wang X, Kleist D T, Lei T. 2021. A simultaneous multiscale data assimilation using scale-dependent localization in GSI-based hybrid 4DEnVar for NCEP FV3-based GFS. Mon Weather Rev, 149: 479–501
Judt F. 2020. Atmospheric predictability of the tropics, middle latitudes, and polar regions explored through global storm-resolving simulations. J Atmos Sci, 77: 257–276
Jung T, Gordon N D, Bauer P, Bromwich D H, Chevallier M, Day J J, Dawson J, Doblas-Reyes F, Fairall C, Goessling H F, Holland M, Inoue J, Iversen T, Klebe S, Lemke P, Losch M, Makshtas A, Mills B, Nurmi P, Perovich D, Reid P, Renfrew I A, Smith G, Svensson G, Tolstykh M, Yang Q. 2016. Advancing polar prediction capabilities on daily to seasonal time scales. Bull Am Meteorol Soc, 97: 1631–1647
Kalnay E. 2002. Atmospheric Modeling, Data Assimilation, and Predictability. Cambridge: Cambridge University Press. 341
Karspeck A R, Yeager S, Danabasoglu G, Hoar T, Collins N, Raeder K, Anderson J, Tribbia J. 2013. An ensemble adjustment kalman filter for the CCSM4 ocean component. J Clim, 26: 7392–7413
Laloyaux P, Balmaseda M, Dee D, Mogensen K, Janssen P. 2016. A coupled data assimilation system for climate reanalysis. Quart J R Meteoro Soc, 142: 65–78
Lei L, Wang Z, Tan Z M. 2021. Integrated hybrid data assimilation for an ensemble kalman filter. Mon Weather Rev, 149: 4091–4105
Li J, Geer A J, Okamoto K, Otkin J A, Liu Z, Han W, Wang P. 2021. Satellite all-sky infrared radiance assimilation: Recent progress and future perspectives. Adv Atmos Sci, 39: 9–21
Li Z, McWilliams J C, Ide K, Farrara J D. 2015. A multiscale variational data assimilation scheme: Formulation and illustration. Mon Weather Rev, 143: 3804–3822
Lorenz E N. 1969a. Three approaches to atmospheric predictability. Bull Amer Meteor Soc, 50: 345–349
Lorenz E N. 1969b. The predictability of a flow which possesses many scales of motion. Tellus A-Dynamic Meteor Oceanography, 21: 289–307
Lorenz E N. 2005. Designing chaotic models. J Atmos Sci, 62: 1574–1587
Lu F, Liu Z, Zhang S, Liu Y. 2015a. Strongly coupled data assimilation using leading averaged coupled covariance (LACC). Part I: Simple model study. Mon Weather Rev, 143: 3823–3837
Lu F, Liu Z, Zhang S, Liu Y, Jacob R. 2015b. Strongly coupled data assimilation using leading averaged coupled covariance (LACC). Part II: CGCM experiments. Mon Weather Rev, 143: 4645–4659
Lucarini V, Blender R, Herbert C, Ragone F, Pascale S, Wouters J. 2014. Mathematical and physical ideas for climate science. Rev Geophys, 52: 809–859
Massonnet F, Mathiot P, Fichefet T, Goosse H, König Beatty C, Vancoppenolle M, Lavergne T. 2013. A model reconstruction of the Antarctic sea ice thickness and volume changes over 1980–2008 using data assimilation. Ocean Model, 64: 67–75
Matsikaris A, Widmann M, Jungclaus J. 2015. On-line and off-line data assimilation in palaeoclimatology: A case study. Clim Past, 11: 81–93
Meehl G A, Goddard L, Murphy J, Stouffer R J, Boer G, Danabasoglu G, Dixon K, Giorgetta M A, Greene A M, Hawkins E, Hegerl G, Karoly D, Keenlyside N, Kimoto M, Kirtman B, Navarra A, Pulwarty R, Smith D, Stammer D, Stockdale T. 2009. Decadal prediction. Bull Amer Meteor Soc, 90: 1467–1486
Mochizuki T, Masuda S, Ishikawa Y, Awaji T. 2016. Multiyear climate prediction with initialization based on 4D-Var data assimilation. Geophys Res Lett, 43: 3903–3910
Palmer T N, Doblas-Reyes F J, Weisheimer A, Rodwell M J. 2008. Toward Seamless prediction: Calibration of climate change projections using seasonal forecasts. Bull Amer Meteor Soc, 89: 459–470
Penny S G. 2014. The hybrid local ensemble transform Kalman filter. Mon Weather Rev, 142: 2139–2149
Penny S G, Hamill T M. 2017. Coupled data assimilation for integrated Earth system analysis and prediction. Bull Am Meteorol Soc, 98: ES169–ES172
Poli P, Healy S B, Dee D P. 2010. Assimilation of Global Positioning System radio occultation data in the ECMWF ERA-Interim reanalysis. Quart J R Meteoro Soc, 136: 1972–1990
Rawlins F, Ballard S P, Bovis K J, Clayton A M, Li D, Inverarity G W, Lorenc A C, Payne T J. 2007. The Met Office global four-dimensional variational data assimilation scheme. Quart J R Meteoro Soc, 133: 347–362
Ruti P M, Tarasova O, Keller J H, Carmichael G, Hov Ø, Jones S C, Terblanche D, Anderson-Lefale C, Barros A P, Bauer P, Bouchet V, Brasseur G, Brunet G, DeCola P, Dike V, Kane M D, Gan C, Gurney K R, Hamburg S, Hazeleger W, Jean M, Johnston D, Lewis A, Li P, Liang X, Lucarini V, Lynch A, Manaenkova E, Jae-Cheol N, Ohtake S, Pinardi N, Polcher J, Ritchie E, Sakya A E, Saulo C, Singhee A, Sopaheluwakan A, Steiner A, Thorpe A, Yamaji M. 2020. Advancing research for seamless Earth system prediction. Bull Am Meteorol Soc, 101: E23–E35
Shapiro M, Shukla J, Brunet G, Nobre C, Béland M, Dole R, Trenberth K, Anthes R, Asrar G, Barrie L, Bougeault P, Brasseur G, Burridge D, Busalacchi A, Caughey J, Chen D, Church J, Enomoto T, Hoskins B, Hov Ø, Laing A, Le Treut H, Marotzke J, McBean G, Meehl G, Miller M, Mills B, Mitchell J, Moncrieff M, Nakazawa T, Olafsson H, Palmer T, Parsons D, Rogers D, Simmons A, Troccoli A, Toth Z, Uccellini L, Velden C, Wallace J M. 2010. An earth-system prediction initiative for the twenty-first century. Bull Amer Meteor Soc, 91: 1377–1388

Sun H, Lei L, Liu Z, Ning L, Tan Z. 2022. An analog offline EnKF for paleoclimate data assimilation. J Adv Model Earth Syst, 14: e2021MS002674

Sun J, Liu Z, Lu F, Zhang W, Zhang S. 2020. Strongly coupled data assimilation using leading averaged coupled covariance (LACC). Part III: Assimilation of real world reanalysis. Mon Weather Rev, 148: 2351–2364

Tan Z M, Zhang F, Rotunno R, Snyder C. 2004. Mesoscale predictability of moist baroclinic waves: Experiments with parameterized convection. Mon Weather Rev, 61: 1794–1804

Tardif R, Hakim G J, Snyder C. 2014. Coupled atmosphere-ocean data assimilation experiments with a low-order climate model. Clim Dyn, 43: 1631–1643

Tardif R, Hakim G J, Snyder C. 2015. Coupled atmosphere-ocean data assimilation experiments with a low-order model and CMIP5 model data. Clim Dyn, 45: 1415–1427

Tong M, Sippel J A, Tallapragada V, Liu E, Kieu C, Kwon I H, Wang W, Liu Q, Ling Y, Zhang B. 2018. Impact of assimilating aircraft reconnaissance observations on tropical cyclone initialization and prediction using operational HWRF and GSI ensemble-variational hybrid data assimilation. Mon Weather Rev, 146: 4155–4177

Whitaker J S, Hamill T M, Wei X, Song Y, Toth Z. 2008. Ensemble data assimilation with the NCEP global forecast system. Mon Weather Rev, 136: 463–482

Xie Y, Koch S, McGinley J, Albers S, Bieringer P E, Wolfson M, Chan M. 2011. A space-time multiscale analysis system: A sequential variational analysis approach. Mon Weather Rev, 139: 1224–1240

Yang X, Rosati A, Zhang S, Delworth T L, Gudgel R G, Zhang R, Vecchi G, Anderson W, Chang Y S, DelSole T, Dixon K, Msadek R, Stern W F, Wittenberg A, Zeng F. 2013. A predictable AMO-like pattern in the GFDL fully coupled ensemble initialization and decadal forecasting system. J Clim, 26: 650–661

Zeng Y, Janjić T, de Lozar A, Welzbacher C A, Blahak U, Seifert A. 2021. Assimilating radar radial wind and reflectivity data in an idealized setup of the COSMO-KENDA system. Atmos Res, 249: 105282

Zhang F. 2005. Dynamics and structure of mesoscale error covariance of a winter cyclone estimated through short-range ensemble forecasts. Mon Weather Rev, 133: 2876–2893

Zhang F, Bei N, Rotunno R, Snyder C, Epifanio C C. 2007. Mesoscale predictability of moist baroclinic waves: Convection-permitting experiments and multistage error growth dynamics. J Atmos Sci, 64: 3579–3594

Zhang F, Weng Y, Sippel J A, Meng Z, Bishop C H. 2009. Cloud-resolving hurricane initialization and prediction through assimilation of doppler radar observations with an ensemble Kalman filter. Mon Wea Rev, 137: 2105–2125

Zhang F, Sun Y Q, Magnusson L, Buizza R, Lin S J, Chen J H, Emanuel K. 2019. What is the predictability limit of midlatitude weather? J Atmos Sci, 76: 1077–1091

Zhang S. 2011. A study of impacts of coupled model initial shocks and state-parameter optimization on climate predictions using a simple pycnocline prediction model. J Clim, 24: 6210–6226

(Editorial handling: Wansuo DUAN)